

PNNL-38394

# Proposed Strategy for Mitigation of Fluid Inclusions in Molten Salt Precursor Materials

September 2025

Kyle Makovsky Michaella Harris Ji-Hye Seo Kent Detrick David Schnable Suhee Choi Jakob Johnson



#### **DISCLAIMER**

This report was prepared as an account of work sponsored by an agency of the United States Government. Neither the United States Government nor any agency thereof, nor Battelle Memorial Institute, nor any of their employees, makes any warranty, express or implied, or assumes any legal liability or responsibility for the accuracy, completeness, or usefulness of any information, apparatus, product, or process disclosed, or represents that its use would not infringe privately owned rights. Reference herein to any specific commercial product, process, or service by trade name, trademark, manufacturer, or otherwise does not necessarily constitute or imply its endorsement, recommendation, or favoring by the United States Government or any agency thereof, or Battelle Memorial Institute. The views and opinions of authors expressed herein do not necessarily state or reflect those of the United States Government or any agency thereof.

PACIFIC NORTHWEST NATIONAL LABORATORY

operated by

BATTELLE

for the

UNITED STATES DEPARTMENT OF ENERGY

under Contract DE-AC05-76RL01830

Printed in the United States of America

Available to DOE and DOE contractors from the Office of Scientific and Technical Information, P.O. Box 62, Oak Ridge, TN 37831-0062

www.osti.gov ph: (865) 576-8401 fox: (865) 576-5728 email: reports@osti.gov

Available to the public from the National Technical Information Service 5301 Shawnee Rd., Alexandria, VA 22312 ph: (800) 553-NTIS (6847) or (703) 605-6000

email: <a href="mailto:info@ntis.gov">info@ntis.gov</a>
Online ordering: <a href="mailto:http://www.ntis.gov">http://www.ntis.gov</a>

# Proposed Strategy for Mitigation of Fluid Inclusions in Molten Salt Precursor Materials

September 2025

Kyle Makovsky Michaella Harris Ji-Hye Seo Kent Detrick David Schnable Suhee Choi Jakob Johnson

Prepared for the U.S. Department of Energy under Contract DE-AC05-76RL01830

Pacific Northwest National Laboratory Richland, Washington 99354

# **Abstract**

The fidelity of experimental data pertaining to thermophysical properties can be directly related to the purity of the materials tested. Water (including OH species) and oxygen are two of the primary non-metallic impurities present in alkali and alkaline earth halide salts. It is generally recognized these halide salts are either hygroscopic or react with oxygenated atmosphere to form hydroxide or oxide species. With respect to water, most previous work has focused on either adsorbed or absorbed water, which conspire to necessitate careful storage, handling, and preparation of these materials for experimental analysis. Born out of the first author's prior experience with geologic minerals, it was hypothesized that synthetic analogues to natural mineral phases (e.g., NaCl- halite, KCl- sylvite, etc.) are susceptible to the incorporation of fluid inclusions. Indeed, in this work we identify fluid inclusions in nearly every commercially produced chloride salt examined, even those advertised as ultra-dry. Thus, we present a brief overview of the processes leading to fluid inclusion development within a single crystal, a preliminary novel approach to estimating their volume, a method to non-destructively verify their contents, and propose a method in which to mitigate their effects on subsequent thermophysical property analysis. Lastly, a comparison is presented between the melting points of precursor and purified salts, examining the efficacy of the method and implications for future research.

Abstract

# **Acronyms and Abbreviations**

DTA Differential Thermal Analysis

DPM Degrees per minute
ML Machine Learning
MSR Molten Salt Reactor

PNNL Pacific Northwest National Laboratory

STA Simultaneous Thermal Analyzer

TGA Thermogravimetric analysis
TMA Thermomechanical analysis

UHP Ultra-high purity XRD X-ray Diffraction

# **Contents**

Abstra	ct			1		
Acrony	yms a	and Abbrev	viations	ii		
1.0 Introduction						
2.0	Experimental Approach					
	2.1	Fluid Ir	Fluid Inclusion Identification and Characterization			
		2.1.1	Optical Microscopy and ImageJ Analysis	3		
		2.1.2	Model Development/Training	3		
		2.1.3	Micro Raman	∠		
	2.2	Host M	laterial Characterization	∠		
		2.2.1	Melting Point			
		2.2.2	Phase Purity	5		
	2.3	Purifica	ation for Melting Point Analysis	6		
3.0	Resi	ults and Di	scussion			
	3.1	Determ	ination of Fluid Inclusion Volume			
	3.2	Identifi	cation of Fluid Inclusion Chemistry	10		
		3.2.1	Micro Raman Analysis of NaCl-1 Fluid Inclusions	10		
		3.2.2	Micro Raman Analysis of KCl-1 Inclusions	13		
	3.3	Salt Pu	rification	15		
	3.4	Determ	ination of Melting Point	18		
4.0	Con	clusions		22		
5.0	Refe	erences		23		
Figu	res	•				
Figure	1. Pł	inclusio	graph of NaCl-1 Grain 1 viewed under transmitted light. Fluid ons are evidenced by the numerous rectangular objects containing al gas bubbles.			
Figure	2. In	segmen First ap	anual fluid inclusion segmentation. (a) Outlined fluid inclusion at compared to grain. (b) Closeup of fluid inclusion segment. (c) spearance of fluid inclusion in image sequence. (d) Last appearance sequence.	8		
Figure	3. M	L-derived	segmentation from KCl (left) and NaCl (right)	9		
Figure	4: Ez		nge Raman scattering spectra collected from various locations, both	11		

Contents

on the surface and centered on three NaCl-1 inclusions	12
Figure 6: Raman depth series data collected from NaCl-1 inclusion 3	12
Figure 7. Bright-field optical images (50× magnification objective) of KCl-1 (top left) grain 2 inclusion 1, (top right) grain 3 inclusion 1, (middle left) grain 4 inclusion 1, (middle right) grain 4 inclusion 2, and (bottom) grain 4 inclusion 3	13
Figure 8: Extended-range Raman scattering spectra collected from various inclusions within KCl-1 grains	14
Figure 9: Water-region Raman scattering spectra collected from various inclusions within KCl-1 grains	14
Figure 10: (top) Raman scattering depth series data collected from KCl-1 grain 2 inclusion 1 and (bottom) optical image of KCl-1 grain 2 inclusion 1 at 50x magnification.	15
Figure 11. Photomicrographs showing fluid inclusions after drying by vacuum oven	15
Figure 12. Titration profile for KCl (a) and NaCl (b). Photomicrographs of single grains of purified KCl (c) and NaCl (d) by hydrochlorination. No fluid inclusions were identified under transmitted light.	17
Figure 13. XRD scans of purified NaCl-2 (top) and KCl-1 (bottom) with hkl lines for peak identification in orange	18
Figure 14. Melting point determined by DTA for a) NaCl-2, b) NaCl-2 Purified, c) KCl-1, and d) KCl-1 Purified. Multiple melting points annotated in the top panel but apply to all panels	19
Figure 15. Melting point determined by TMA for a) NaCl-1 and b) NaCl-2 Purified.  Positions in dL/Lo curve (red) showing melting point are annotated	20
Tables	
Table 1. Operating Parameters for XRD phase purity characterization	5
Table 2. Results of calculated fluid inclusion volumes and volume fraction.	10
Table 3. Comparison of measured melting points between DTA and TMA, respectively	21

Tables

# 1.0 Introduction

Molten Salt Reactors (MSRs) utilize complex mixtures of either chlorides or fluorides which contain fissile components to produce heat for power production. Non-fissile mixtures may also be used as a medium for heat transfer and thermal regulation of the reactor. A thorough understanding of their physical properties is required for these systems to operate predictably, efficiently, and safely. To support this requirement, PNNL is engaged in developing techniques for measuring thermophysical properties and providing fundamental data for various salt mixtures. These data may then be utilized by MSR developers to advance their individual R&D efforts.

Water plays a critical role in modifying the physical properties of materials. For example, it has been shown that water affects the chemical stability and corrosion behavior of molten chloride salts (Fernandez and Cabeza, 2020; Raiman et al., 2021; Rippy et al., 2023). Thermal dehydration catalyzes hydrolysis in hygroscopic salts, leading to the formation of secondary chemical species that in turn affect its thermophysical properties. Because of this, significant efforts have been made to reduce exposure of salt to water and oxygen (e.g., PNNL-37190) and in developing purification methods (Maricle and Hume, 1960; Indacochea et al., 1998; Witteman et al., 2023). Although these methods are adequate at mitigating impurities in the molten state through on-line monitoring and purification, there exists other potential sources of water contamination in precursor materials that are relevant for benchtop-scale measurements.

The work herein documents for the first time the existence of fluid inclusions in synthetic precursor salts used for thermophysical property measurements. Inclusions in general may be defined as "a part of a crystal, not part of its regular structure" (Hurai et al., 2015). Fluid inclusions then are pockets of fluid trapped in a single crystal which may include only gas, a gasliquid mixture, or only liquid. These features are ubiquitous in minerals formed in many geologic environments (Roedder, 1984; Hurai et al., 2015). In the field of experimental petrology, mineral analogues are routinely synthesized with fluid inclusions to better understand their behavior in natural minerals (e.g., Bodnar et al., 1985). As such, they provide the only direct evidence of the fluid and its chemical and physical condition at the time the mineral was precipitated, allowing geologists to reconstruct past environments. In this context their existence may be viewed favorably. Conversely, they may be viewed as troublesome impurities in areas where chemical purity is extremely important, such as the pharmaceutical industry (e.g., Marc et al., 2021) and in the manufacture of explosives (e.g., Cooper et al., 2020). In this work, the former stance is taken as the goal is to produce fundamental thermophysical property data of the highest fidelity.

Fluid inclusions are features previously unrecognized in molten salt precursor materials. Although inclusions were identified in several chlorides and fluorides, this report focuses on those in NaCl and KCl. Other salts will be examined in detail along with those presented here in subsequent peer-reviewed journal articles. The overall goal of the work here was to identify a method in which to mitigate the effects of fluid inclusions on benchtop-scale thermophysical property measurements. To do this, techniques were developed to identify and characterize their size and total volume. Next, using methods previously established in the geoscience community, develop the capability at PNNL to measure the chemistry of fluid inclusions using micro-Raman spectroscopy. Next, two techniques to rid precursor materials of water were explored. Lastly, the

Introduction 1

melting point of non-purified and purified salts were measured to determine the effect, if any, of fluid inclusions on the measured thermophysical properties.

Introduction 2

# 2.0 Experimental Approach

#### 2.1 Fluid Inclusion Identification and Characterization

# 2.1.1 Optical Microscopy and ImageJ Analysis

A Keyence VHX-7000 digital microscope (Keyence Corporation of America, Itasca, IL.) was used to capture images of single salt grains and their respective content of fluid inclusions. In this study a grain is defined as a single particle from the bulk powder, with no distinction made between grains that are mono- or polycrystalline. Images were captured under transmitted light with varying magnifications (x500-x2500) depending on grain size and depth of inclusions. Using the depth profile function in the microscope software a 3D image was captured to determine volume of the grain. Images were captured in 0.5-2 µm increments depending on the grain size to determine height of the fluid inclusions. Using ImageJ (LOCI, University of Wisconsin) the cross-section surface area of the fluid inclusion was determined. Surface area was calculated by tracing the cross-sectional boundaries and converting pixel to distance. When paired with the first and last appearance of the inclusion via the measured images the total volume of the inclusion was resolved. The pixel to distance conversion was done by measuring the scale bar in ImageJ and dividing the micron scale by the length in pixels.

#### 2.1.2 Model Development/Training

To automate the identification and volume computation of fluid inclusions, a machine learning (ML)-based method was developed. The developed framework takes inspiration from MoCo (He et al., 2020), a state-of-the-art self-supervised model framework. A ResNet-50 (He et al., 2015) encoder was used as a backbone, initialized with filters pretrained on ImageNet (Russakovsky et al., 2015). The encoder model is trained using the MoCo training method using the large unlabeled dataset. This model is trained to convergence, which took 150 epochs. The encoder is then attached to a decoder similar to UNet's (Ronneberger et al., 2015), with skip connections at each pooling layer of the ResNet architecture. The whole model (encoder and decoder) is then trained for 150 epochs until convergence. During encoder training MoCo's suggested augmentations was used and randomly cropped the input image to 256×256. For decoder training, the same augmentations were used and add random erasing to reduce overfitting. The final predicted labels are upscaled to the original 2880×2160 resolution for final volume calculation.

To compute the volume of the predicted inclusions, the pixel width and height between slices were used with equation 1 to compute the total volume V of the inclusions in the grain.

$$V = \sum_{i=0}^{N} \sum_{j=0}^{M} h \times p^2 \times x_j$$
 (1)

Where N is the number of slices, M is the number of pixels, h is the slice height in  $\mu m$ , p is pixel width in  $\mu m$ , and  $x_i \in \{0, 1\}$  is the pixel prediction.

#### 2.1.3 Micro Raman

Normal-Stokes Raman scattering spectra were collected using a Renishaw inVia<sup>TM</sup> confocal Raman microscope using a 50× magnification objective and motorized stage. Incident light was provided by a 488 nm class 3B laser (Renishaw RL-488, 200 mW continuous power). Transmitted laser power was reduced using a series of neutral density filters resulting in nominally 2.5% light transmission to the sample. Scattered light was projected across a Renishaw Centrus CCD detector via a motorized variable-angle diffraction grating (1800 gr./mm). Spectra requiring multiple collections due to wide spectral range were collected in segments and stitched together using Renishaw's SynchroScan® technology. Prior to data collection, wavenumber calibration was referenced to the Raman scattering band of an internal silicon standard (520.5 cm<sup>-1</sup>).

A series of grains were affixed to a glass slide using double sided tape. Within each grain, multiple inclusions were probed via Raman spectroscopy to investigate the contents of each inclusion. Depth measurements were performed by varying sampling coordinates along the Z-axis to confirm that the observed signals originate from the inclusions themselves, rather than the regions above or below it. Similarly, blank spectra were collected from the grain surface to further corroborate the origin of the observed Raman scattering bands.

#### 2.2 Host Material Characterization

All salts in this study used for characterization or thermophysical property measurement were stored and prepped for analysis in an inert atmosphere glovebox (nominal  $H_2O \sim 1$  ppm;  $O_2$ - 1 ppm). Where possible, salts were transported to the site of analysis using a vacuum sample transfer vessel.

#### 2.2.1 Melting Point

Two methods were used to determine the melting point of as received and purified salts. Each method has its strengths and limitations, thus the aim was to reduce potential bias from either and to verify they converged on a singular value, within uncertainty of each method.

#### 2.2.1.1 Thermomechanical Analysis (TMA)

Powdered salt was weighed into 0.25 g samples. Each sample was pressed into a green compact using a 6 mm die and mechanical Carver hand press. The samples were loaded into a crucible and plunger set. The assembled sample container was loaded into a small vacuum sealed container and transported to the TMA. The TMA instrument is on a benchtop and does not have a method of controlling the atmosphere while the sample is loaded. Therefore, the sample was quickly removed from the small vacuum sealed container, loaded into the TMA, and placed under an argon atmosphere to prevent gross oxygen and water contamination of the sample.

The melting point determination for the salts and temperature calibration metals were done using the technique given by ASTM E1363-23. Salt melting points used a force of 25 mN for these determinations and for the metals a force of 50 mN was used.

The temperature measurement was taken by a thermocouple that was placed close to the outer wall of the crucible without touching the crucible (<2 mm). A temperature calibration was built using 99.999% pure metal sample supplied by NETZSCH for this purpose. The regression calibration used In, Pb, Sn, Ag, Bi, and Al, with all metals weighted as 1 except indium weighted as 10 by software default. The 95% confidence single-point prediction band estimates the temperature measurement error as about  $\pm 3.8$ °C at the most.

The temperature program for each of the salts measured used a ramp rate of 10 K/min. The temperature was ramped up to 900 °C for both KCl and NaCl. Then the temperature was cycled between the maximum temperature and about 100°C below the melting point for a total of 4 ramp and cool cycles. Before initiating temperature ramps the furnace was evacuated and filled with ultra-high purity argon passed through an additional oxygen and water getter. The sample crucible was placed on a flat alumina pushrod that controlled the applied force on the sample at 25 mN for the full duration of the measurement. The upper anvil was an alumina wedge that contacted the top of the plunger.

#### 2.2.1.2 Differential Thermal Analysis (DTA)

Powdered salt was weighed into  $\sim\!20$  mg samples. Silver crucibles were used as the sample holders and the baseline. The crucibles were loaded into a NETZSCH simultaneous thermal analyzer (STA) equipped with the DTA sensor with protected thermocouple sample carrier. The temperature program consisted of 7 segments. All segments had a ramp rate of 10 °C/min and 5-minute dwell when the target temperature was reached. Segments cycled between 715 °C to 850°C to capture the melting point onset. Samples were run under argon with a carrier rate of 40 mL/min.

A temperature calibration was performed with In, Zn, and BaCO<sub>3</sub>. The operating parameters for the temperature calibration was a ramp through the melting range to 100 °C past the melting point. The temperature correction was applied in a similar way as described in 2.2.1.1.

#### 2.2.2 Phase Purity

A Bruker D8 X-ray Diffractometer (XRD) (Bruker, Billerica, MA) was used for data acquisition. Samples were packed into an inert dome holder to prevent water and oxygen adsorption to the material. Running parameters are listed in Table 1.

Table 1. Operating Parameters for XRD phase purity characterization

Operational Parameters	Setting
2θ Range	5-90
Step Size (°)	0.02
Step Rate (dpm)	1

XRD scans were analyzed using DIFFRAC.EVA (Bruker, Billerica, MA) software. For the purposes of this work only phase identification was needed.

# 2.3 Purification for Melting Point Analysis

Salts were purchased from several vendors. They ranged in metal basis purity and vendor-reported water content.

Dehydration and hydrochlorination were performed on both KCl and NaCl to remove water, oxide ions, and hydroxide ions from the salts. Approximately 20 g of salt was loaded in a 100 mL high-purity alumina crucible (AdValue Technology) placed inside a quartz vessel. Quartz wool (AdValue Technology) was placed on top of the quartz reactor for thermal insulation. A custom-made Teflon lid was clamped to seal the quartz vessel, and a thermocouple inserted into the quartz vessel was used to monitor the temperature inside the vessel. An alumina tube was inserted into the reactor to introduce ultra-high-purity (UHP) Ar and/or anhydrous HCl gas.

The vessel was connected to a vacuum pump and heated to 200 °C at a rate of 250 °C/h and held for an hour to remove moisture. A dry ice trap was used to protect the vacuum pump from moisture. After one hour, the vacuum was disconnected and replaced with UHP Ar gas flowing at 50 mL/min. The temperature was further increased to the melting point, and the UHP Ar gas flow was increased to 90 mL/min. It was heated up to 770 °C and 900 °C for KCl and NaCl, respectively. Then the 100% HCl gas was flowed at 40-70mL/min mixed with 90 mL/min UHP Ar for up to 2 h. During the hydrochlorination step of the salt purification process, the effluent gas coming out of the quartz reactor was bubbled into a titration cell connected to a TitroLine 7000 auto titrator running in pH state mode (pH=10) using 0.1M NaOH (Fisher Scientific, ≥97%) as the titrant. The function of the auto titrator was to indicate the time at which there was no net HCl gas consumption. Once the impurities were removed, the furnace was allowed to cool to room temperature while UHP Ar was flowed into the vessel at a rate of 50 mL/min. The flow rate was controlled using a rotameter (Omega).

A vacuum oven was used to dry approximately 2 g aliquots of NaCl and KCl. Two temperature profiles were used. First, each 2 g batch was brought to an isothermal hold of 8 hours at 100 °C. After the first hold, the samples were removed from the oven and approximately 100 grains were mounted for examination via optical microscopy. After this analysis the remaining salt was again loaded into the vacuum oven and brought to an isothermal hold for 8 hours at 200 °C. Images were again taken on a small subset of grains from each salt via optical microscopy.

# 3.0 Results and Discussion

The results of the measurements outlined below are anonymized to preclude direct correlation of a particular salt to a specific manufacturer. It is understood that manufacturers likely spend significant time and resources developing in-house expertise and processes to synthesize these materials. Through anonymization, the results presented here address the greater issue of fluid inclusions while eliminating the possibility of unintended negative consequences for any given salt manufacturer.

#### 3.1 Determination of Fluid Inclusion Volume

A depth profile was generated from the base of the grain (top of the glass slide) to the top of the grain. Once generated, the grain was manually traced to calculate the volume and surface area. The depth profile for NaCl-1 Grain 1 was taken in height increments of one micron which were used when determining the height of analyzed fluid inclusions (e.g., Fig. 1).

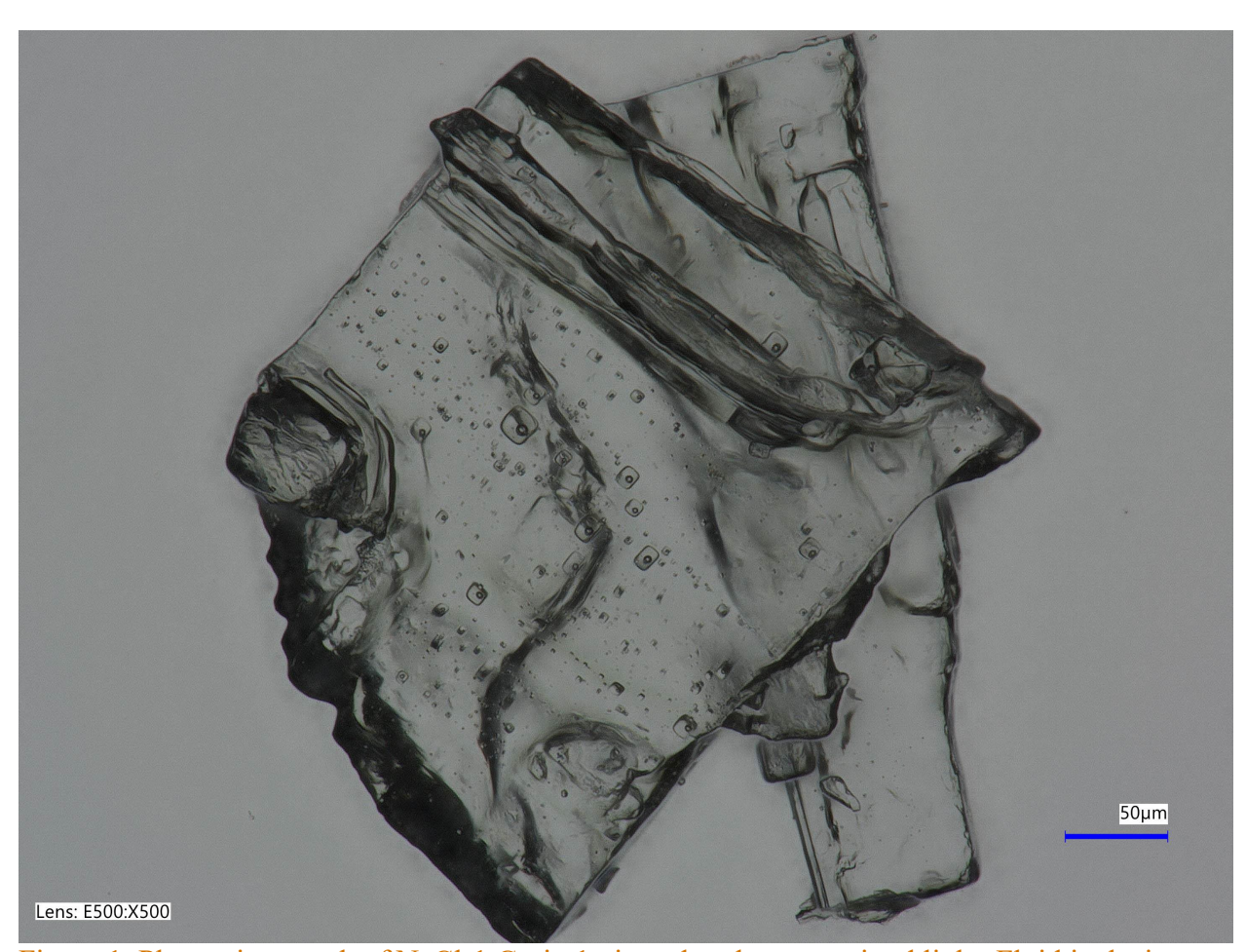


Figure 1. Photomicrograph of NaCl-1 Grain 1 viewed under transmitted light. Fluid inclusions are evidenced by the numerous rectangular objects containing spherical gas bubbles.

Fluid inclusions observed in both NaCl and KCl exhibited a cubic morphology generally identical to the crystal system of their host crystals (Fig. 2). This is a common characteristic

resulting from processes occurring at the crystal growth front during precipitation (Hurai et al., 2015). Most inclusions also contained a gas bubble which was used as a diagnostic indicator that what was being observed was in fact a fluid inclusion. These bubbles are typically formed by the thermal contraction of the fluid phase upon cooling after entrapment, leaving a void space in which dissolved gases in the liquid portion can exsolve, filling the void space. The total volumes calculated by the methods employed here do not account for the volume fraction of the vapor phase within the inclusions.

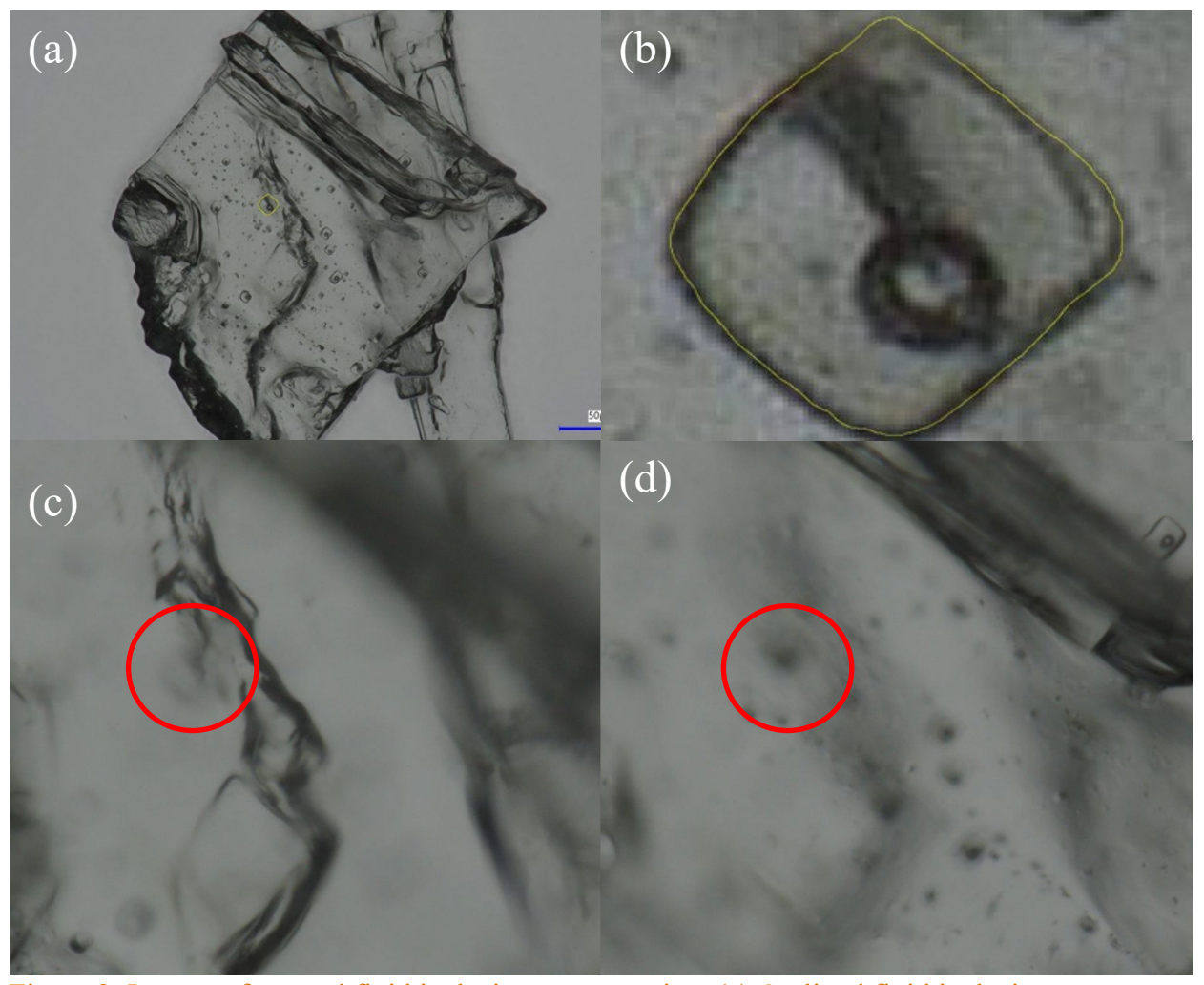
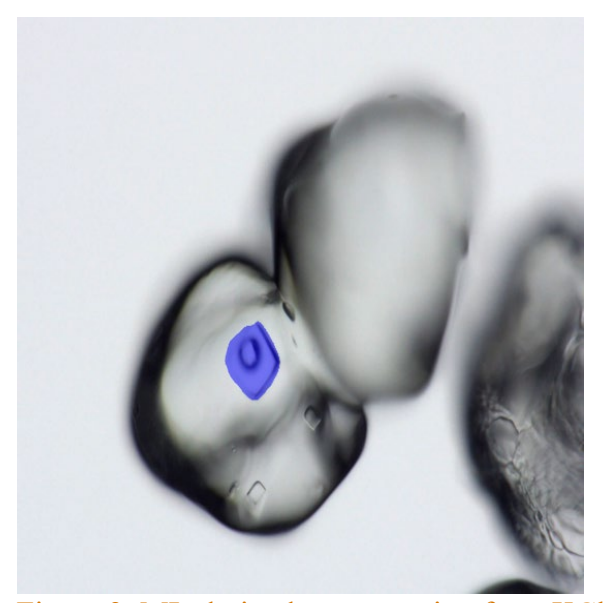


Figure 2. Images of manual fluid inclusion segmentation. (a) Outlined fluid inclusion segment compared to grain. (b) Closeup of fluid inclusion segment. (c) First appearance of fluid inclusion in image sequence. (d) Last appearance in image sequence.

Manual segmentation was found to be extremely labor intensive (Fig. 2b), with a typical analyst investing approximately 6-8 hours per grain depending on the number of inclusions present. Although the results are likely less prone to measurement uncertainty, the required time investment precludes this technique from being scaled up to a meaningful level.

To address this pitfall, an ML approach was developed using well-characterized techniques. Once the workflow was established, the characterization of a single grain was reduced to approximately a few seconds. Nevertheless, the ML results described below should be viewed as preliminary; however, the workflow developed here does provide a foundation upon which future work can be built.

A ML-model was developed to segment a set of salt grains. It was also used to determine the total volume of the two-phase fluid inclusions in the grains. Qualitatively it performs well, segmenting nearly all visible two-phase inclusions (Fig. 3). Some expansion of the inclusions' segmentations is visible, which is hypothesized to be due to up- and down-scaling of the images. Overall, the ML method tended to underestimate the inclusion volume compared to the hand segmentation. The model had difficulty detecting inclusion borders near the top and bottom of the inclusion, when they are very blurry. Another source of error for the model is the downscaling and upscaling of the images. When segmented at lower resolution, large pixels might be unable to correctly represent the inclusion boundary.



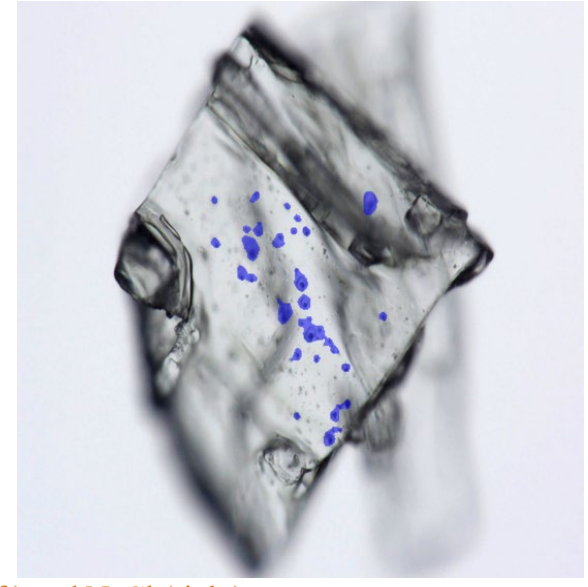


Figure 3. ML-derived segmentation from KCl (left) and NaCl (right).

Dice score was used to determine the performance of our model. This is a common metric used in ML image segmentation. After training, the model Dice scores on the training and validation sets are 0.793 and 0.760, respectively. Visually, segmentation accuracy was good, with some expansion of inclusions into nearby regions.

The results of hand versus ML-derived volumes are presented in Table 2. A limited subset of grains were analyzed by hand due to the time intensive nature of their derivation. However, for those grains where inclusion-host grain pairs exist for the two methods, the results between them generally agree. It is important to note the uncertainties associated with each method were not determined, thus at this time their statistical correlation is uncertain. Variability does exist within a single salt set, ranging between a factor of 2-10. This is consistent with qualitative observations that within a particular salt, not every grain contains an equal number of fluid inclusions.

Table 2. Results of calculated fluid inclusion volumes and volume fraction.

Salt	ML Model Volume (µm³)	Total Volume Fraction (%)	Hand Segmented Volume (µm³)	Total Volume Fraction (%)
NaCI-1 Grain 1	67164.9	0.65	177111.9	1.71
NaCI-1 Grain 2	9736.7	1.79	6006.4	1.10
NaCI-2 Grain 1	13928.3	0.05	N/A	N/A
NaCI-2 Grain 2	6762.6	0.02	N/A	N/A
NaCI-2 Grain 3	9911.7	0.02	N/A	N/A
KCI-1 Grain 1	1735.3	0.11	N/A	N/A
KCI-1 Grain 2	35188.9	1.00	61431.5	1.70
KCI-1 Grain 3	14022.9	0.13	53382.4	0.50
KCI-2 Grain 1	29164.8	0.09	N/A	N/A
KCI-2 Grain 2	4826.8	0.04	N/A	N/A
KCI-2 Grain 3	5149.1	0.11	N/A	N/A

The volume of water calculated (as volume fraction) regardless of the method may have significant implications for the evaluation of thermophysical properties. For example, for NaCl-1 Grain 2, both methods suggest that NaCl-1 Grain 2 contains between 1.10 and 1.79 vol % water. This is a significant contributor to the total impurities potentially present in a salt sample. This will likely become a greater issue for reactor scale-up. For example, in an unpurified 50:50 mixture (by weight) of NaCl-KCl, our results suggest that for every kg of that mixture, one might expect approximately 4.8 g of water to be present (at ~1 vol% water).

# 3.2 Identification of Fluid Inclusion Chemistry

We developed a micro-Raman spectroscopy capability at PNNL to verify that the contents within the identified fluid inclusions were in fact water; Raman spectroscopy is commonly used in the geosciences for this purpose. Individual grains were selected from the bulk NaCl and KCl materials for investigation via Raman vibrational spectroscopy. Raman data were collected from multiple inclusions within each grain using a 488 nm class 3B incident laser and a Renishaw inVia Raman microscope. Initial attempts focused on using grains that were mounted in epoxy on thin sections. However, difficulties detecting Raman scattering from this sample configuration were encountered. We chose instead to mount full grains onto glass slides using two-sided tape. The first sample to be investigated using this sample configuration was NaCl-1, which featured relatively large inclusions (shortest edge generally *ca.* 10 µm) that were facile to measure and allowed for straightforward optimization of the collection parameters.

# 3.2.1 Micro Raman Analysis of NaCl-1 Fluid Inclusions

Raman scattering spectra were collected from NaCl-1 at four locations, including three inclusions, across a broad spectral region (30–5500 cm<sup>-1</sup>) to identify any and all scattering

signals present (Fig. 4). NaCl adopts a high-symmetry centrosymmetric cubic fluorite structure and therefore does not possess any Raman-active vibrational modes under normal conditions. Any Raman signals detected here therefore stem from crystallographic defects or impurities. Data collected from all four measurement locations feature a broad, elevated baseline consistent with background sample fluorescence under excitation at 488 nm (Fig. 4). As NaCl is also not expected to fluoresce, the elevated baseline is likely due either to trace impurities or to the tape/adhesive used to immobilize the sample. The latter is further supported by the presence of a minor Raman band at *ca.* 2900 cm<sup>-1</sup>; signals in this region are typically associated with organic C–H vibrations that would be expected from such adhesives (Fig. 4).

The elevated baseline and broad peak at *ca*. 2900 cm<sup>-1</sup> are the only signals present at the surface of the grain, far from any inclusions (Fig. 4). In contrast, all three inclusions additionally contain a broad signal at *ca*. 3400 cm<sup>-1</sup>. This spectral feature is consistent with the presence of water within these three two-phase inclusions.

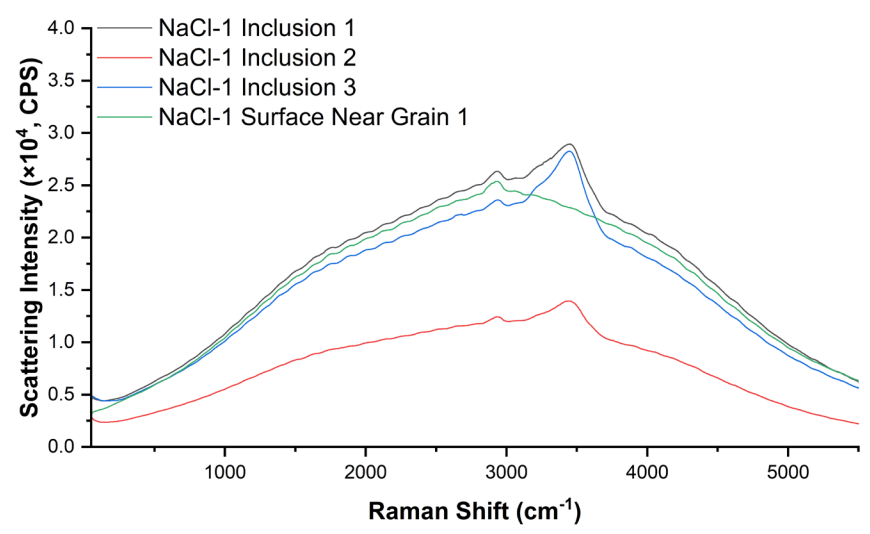


Figure 4: Extended-range Raman scattering spectra collected from various locations, both on the surface and centered on three NaCl-1 inclusions.

Higher resolution data were collected within a narrow region centered at *ca.* 3400 cm<sup>-1</sup> to further interrogate these water-associated features (Fig. 5). This higher quality data enabled Gaussian peak deconvolution of these bands into four components. Similar multicomponent scattering signals have previously been observed from concentrated aqueous solutions of NaCl at room temperature.

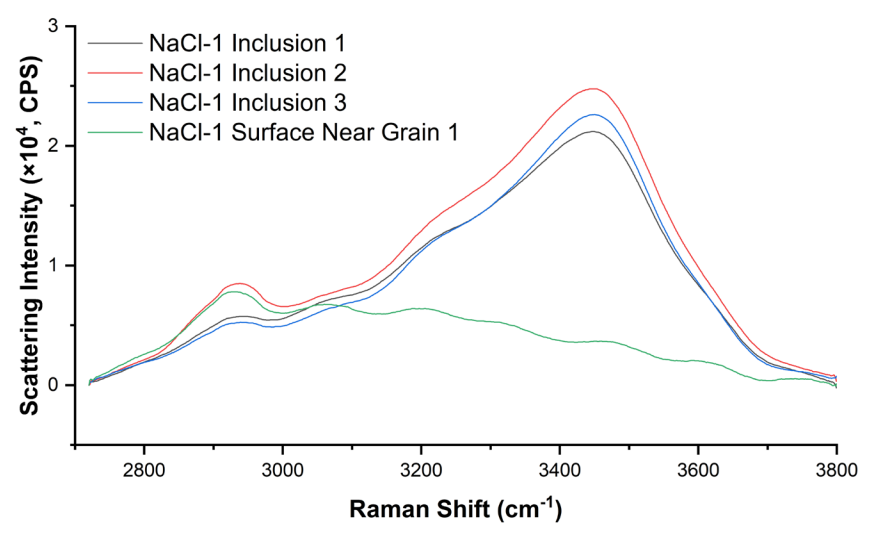


Figure 5: Water-region Raman scattering spectra collected from various locations, both on the surface and centered on three NaCl-1 inclusions.

The absence of these signals at the surface of the grain indicates that these features may arise from the inclusion contents. To confirm this, variable depth Raman measurements were conducted to track the intensity of these spectral features as the sampling area was moved along the Z-axis (height) through the inclusion (Fig. 6). Throughout this measurement, the intensity of the water signal rose then fell, reaching its apex as the sample volume traversed the inclusion. This provides confirmation that these water-associated signals stem from the contents of the inclusion itself, rather than the surrounding region.

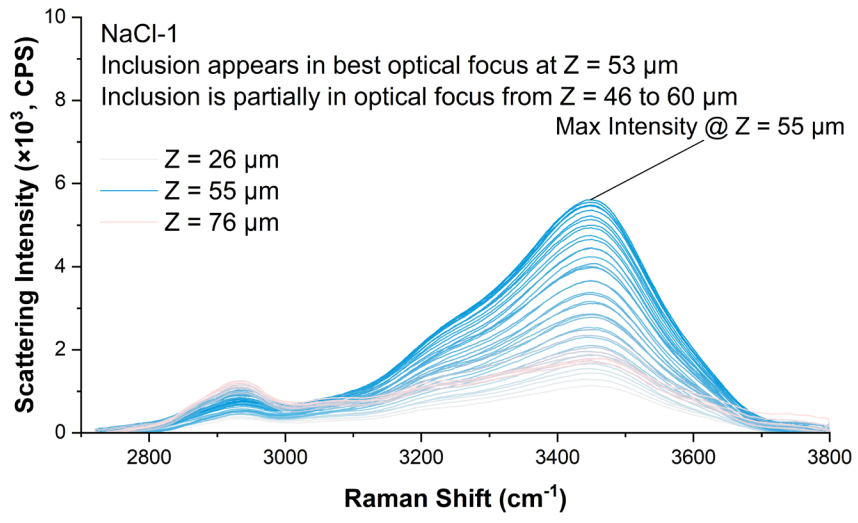


Figure 6: Raman depth series data collected from NaCl-1 inclusion 3.

The signals at ca. 2900 cm<sup>-1</sup> that we previously assigned to organic adhesives consistently intensified as the sample was raised and the sampling volume neared the tape. This is another indication that this feature originates from the adhesives of the tape.

# 3.2.2 Micro Raman Analysis of KCI-1 Inclusions

Four grains from KCl-1 were selected for analysis and again immobilized on a glass slide using double-sided tape. In general, inclusions in the KCl-1 samples were larger than those observed in NaCl-1 (generally longest edge ca.  $>20~\mu m$ ). Optical images from selected inclusions are shown in Figure 7. Unlike the other inclusions investigated thus far, two single-phase inclusions were also targeted for analysis in this case (grain 4, inclusions 2 and 3).

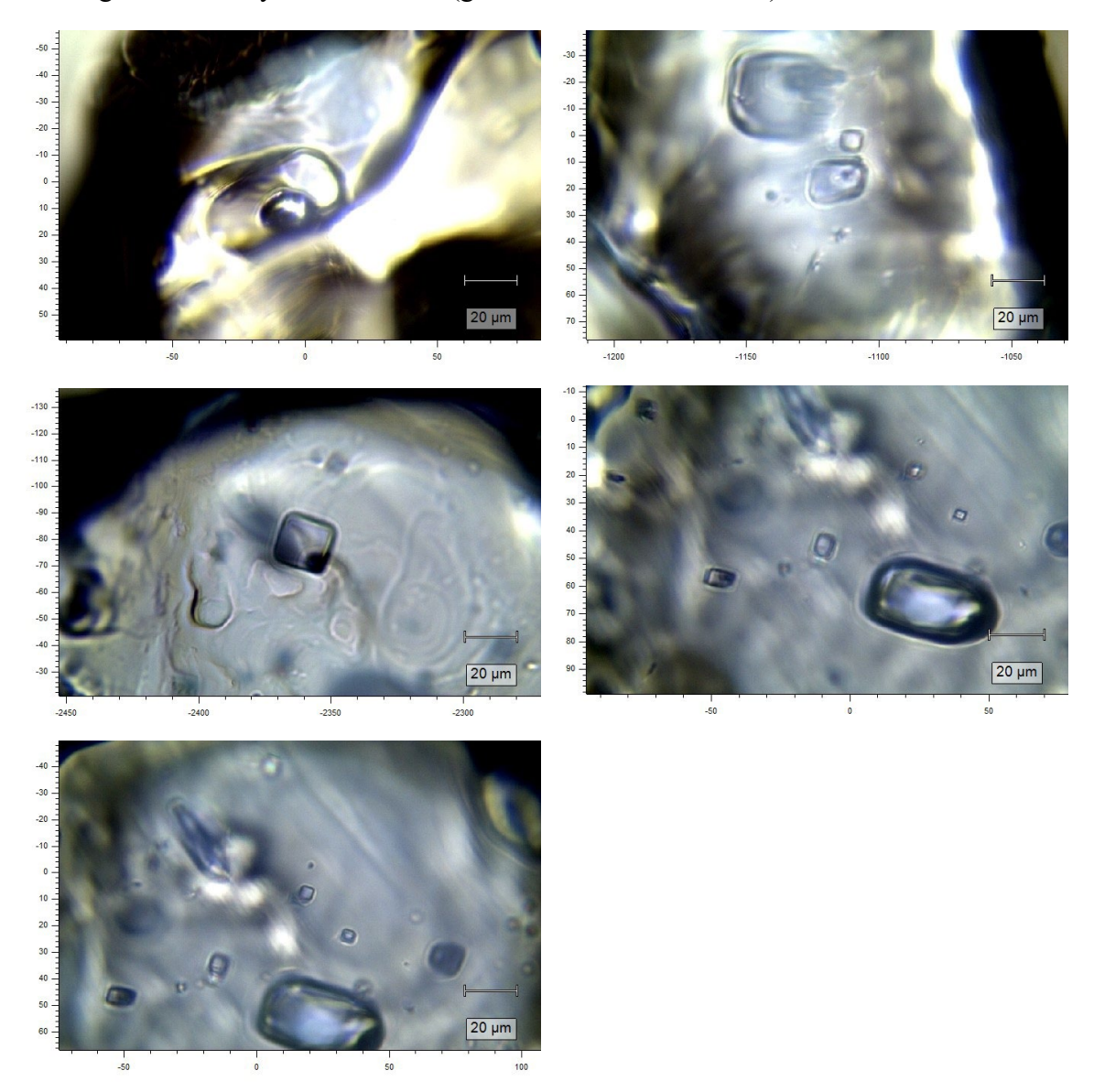


Figure 7. Bright-field optical images (50× magnification objective) of KCl-1 (top left) grain 2 inclusion 1, (top right) grain 3 inclusion 1, (middle left) grain 4 inclusion 1, (middle right) grain 4 inclusion 2, and (bottom) grain 4 inclusion 3.

Wide-region Raman scans (Fig. 8) revealed only the same background fluorescence, plus adhesive- and water-associated signals previously observed in NaCl-1.

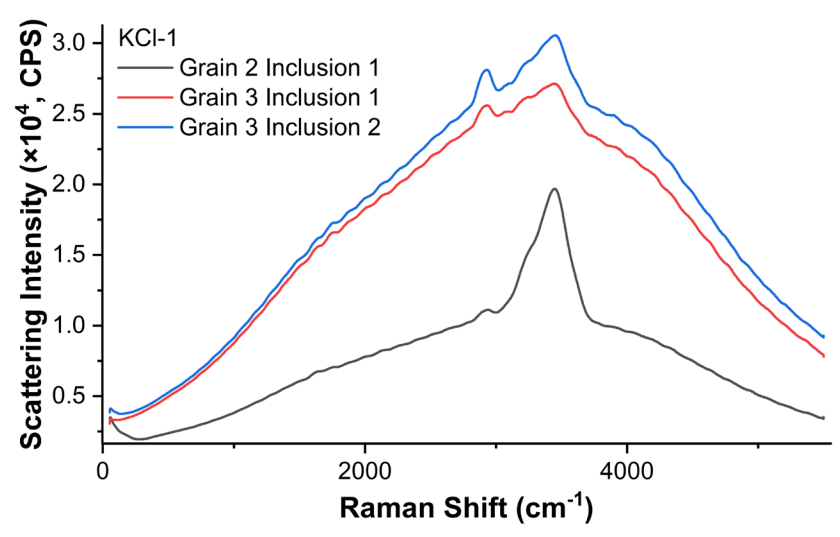


Figure 8: Extended-range Raman scattering spectra collected from various inclusions within KCl-1 grains.

Higher-resolution scans of the *ca.* 3400 cm<sup>-1</sup> region again revealed a four-component water scattering feature (Fig. 9) in all but two of the investigated inclusions. Interestingly, neither of the two single-phase inclusions selected from grain 4 (Fig. 9, inclusions 2 and 3, purple and gold traces) displayed any signals aside from background fluorescence. This indicates that no water was present within these inclusions, a possible sign of decrepitation.

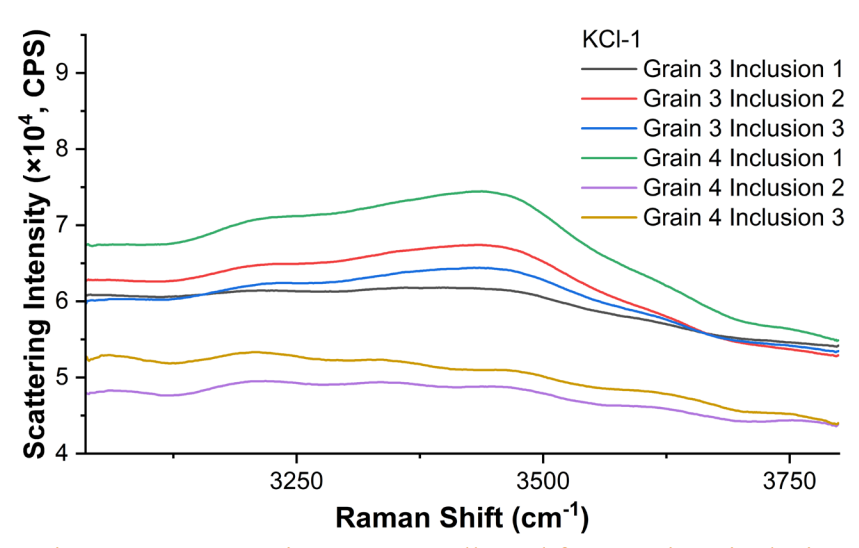


Figure 9: Water-region Raman scattering spectra collected from various inclusions within KCl-1 grains.

Identical variable-depth Raman measurements were conducted on KCl-1 grain 2 inclusion 1 (Fig. 10) and revealed similar behavior to NaCl-1 grain 3 (Fig. 6). The intensity of the water-associated scattering feature in the KCl sample rose and fell commensurately with proximity to the inclusion depth. These results confirm that this 4-component scattering feature again originated from the contents of the inclusion.

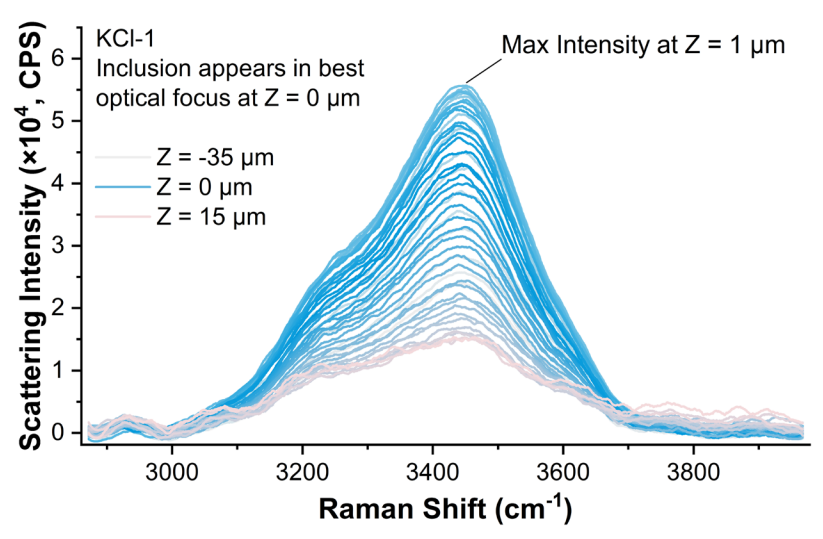


Figure 10: (top) Raman scattering depth series data collected from KCl-1 grain 2 inclusion 1 and (bottom) optical image of KCl-1 grain 2 inclusion 1 at 50x magnification.

#### 3.3 Salt Purification

Vacuum drying in an inert oven is a common method to dehydrate salts prior to analysis. It was hypothesized that this may be an effective method in which to destroy fluid inclusions. In natural minerals however, fluid inclusions have been observed in minerals that have been subjected to temperatures and pressures reaching 10 kb and 1000 °C (van der Kerkhof et al., 2014). Obviously, the main differences between natural minerals the salts considered here are the rates and duration at which they are subjected to these conditions. Nonetheless, if the rate of expansion of the fluid within an inclusion upon heating surpasses the elastic modulus of the host mineral, then it could produce a fracture from which the entrapped fluid can escape. It is reasonable to think this process may occur during rapid heating in a vacuum oven, hence the justification to test this hypothesis.

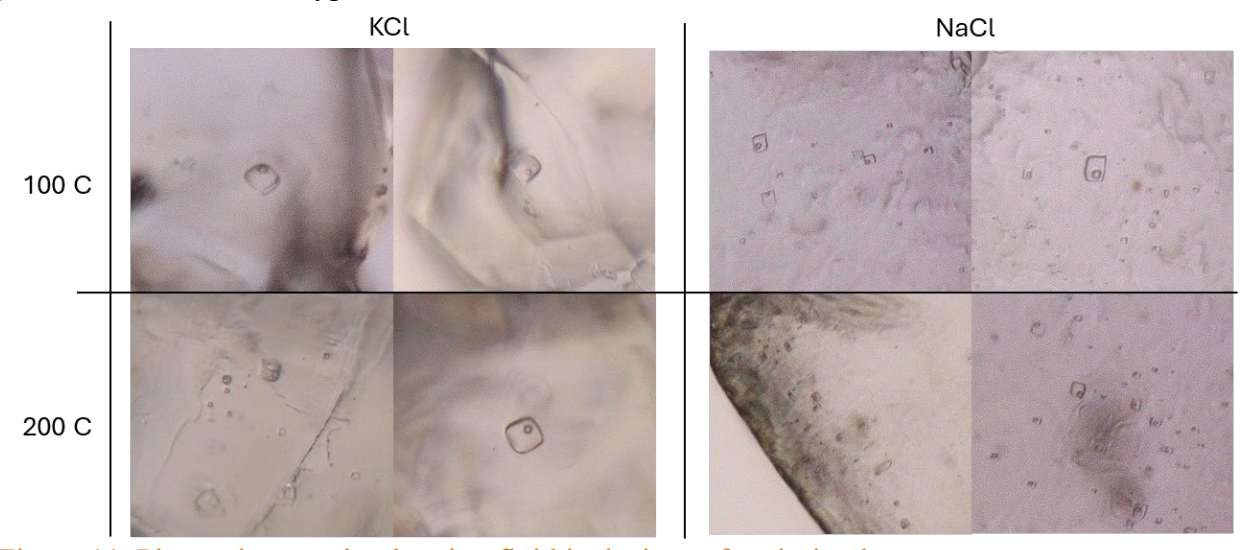


Figure 11. Photomicrographs showing fluid inclusions after drying by vacuum oven.

No observable change in the number or state of fluid inclusions was detected in salts subjected to vacuum oven drying (Fig. 11). The inclusions persisted after being subjected to a total of 16 hours of elevated temperatures, first at 100 °C for 8 hours then 200 °C for an additional 8 hours. Due to this, an alternative method was needed to purify the salts prior to evaluation of melting point.

Hydrochlorination of salt in the molten state was investigated as a potential method to destroy fluid inclusions. Simply melting the salt would destroy the fluid inclusions, but the release of water upon melting likely creates oxides and hydroxides. Thus, it was hypothesized this method would address both these issues.

Real-time monitoring of the hydrochlorination was used to determine how long to run the chlorination. Figure 12 (a) and 12 (b) give the titration plots for the hydrochlorination of KCl and NaCl, respectively. Initially, the feed HCl gas was bypassed around the quartz vessel, directly into the auto-titrator cell. This established the input rate of HCl gas flow (red lines in Figure 12). Then the feed gas was introduced into the vessel to react with impurities in the salt. The reaction of HCl gas with impurities decreases the rate of HCl flowing out in the effluent gas (green lines in Figure 12). The expected reactions are given below (Eq. 2 and Eq. 3).

$$HCl + O^{2-} \rightarrow H_2O + 2Cl^-$$
 (2)

$$HCl + OH^- \rightarrow H_2O + Cl^- \tag{3}$$

When the HCl stops reacting with impurities, its flow rate in the effluent stream should be similar to its flow rate in the feed stream (blue lines in Figure 12). Fig 12 (a) shows the slope (0.06803 mL/min) returning to its initial value (0.06336 mL/min) after about 7 minutes, whereas it took around 4 minutes for the slope (0.14236 mL/min) to return to its initial value (0.16519 mL/min). The difference in the initial values of the flow rates of KCl and NaCl is due to controlling the flow meter for HCl gas.

After purification, aliquots of the salts were interrogated for the presence of fluid inclusions via optical microscopy (Fig. 12 c and d). No fluid inclusions were observed. The crystalline material exhibited high optical clarity making it difficult to observe any internal features. This added confidence to the efficacy of the method.

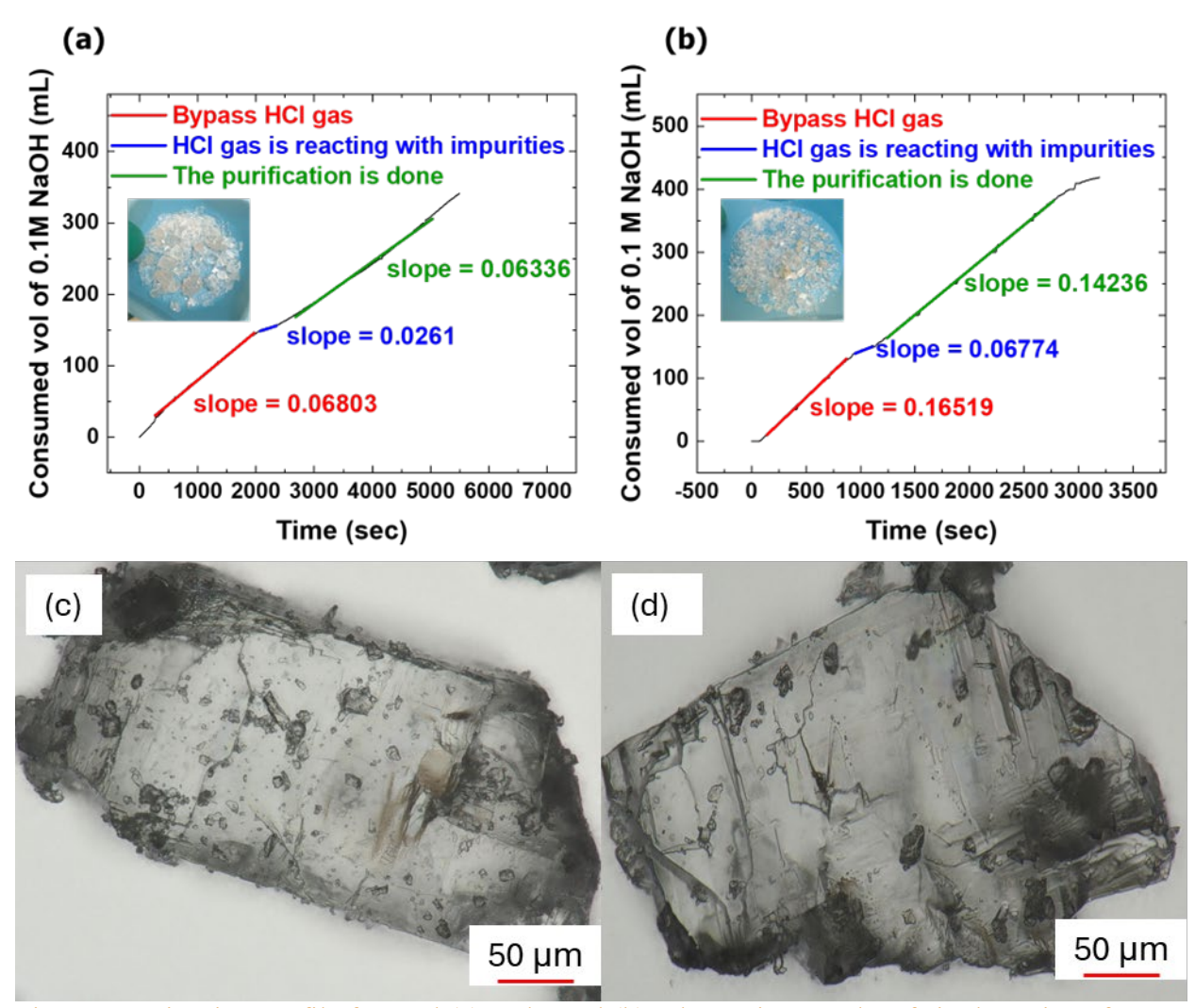


Figure 12. Titration profile for KCl (a) and NaCl (b). Photomicrographs of single grains of purified KCl (c) and NaCl (d) by hydrochlorination. No fluid inclusions were identified under transmitted light.

To confirm the phase purity of the hydrochlorinated salts, x-ray diffraction patterns of an aliquot of each salt were collected. The diffractograms in Figure 13 suggest the samples exhibit high phase purity, at least within the sensitivity of the method to detect impurities. Although not the focus of the micro-Raman analysis, collected spectra on the purified NaCl-2 sample corroborates the XRD results. Because of this, confidence was high that measured thermophysical properties (e.g., melting point) from these samples would be representative of the fundamental value.

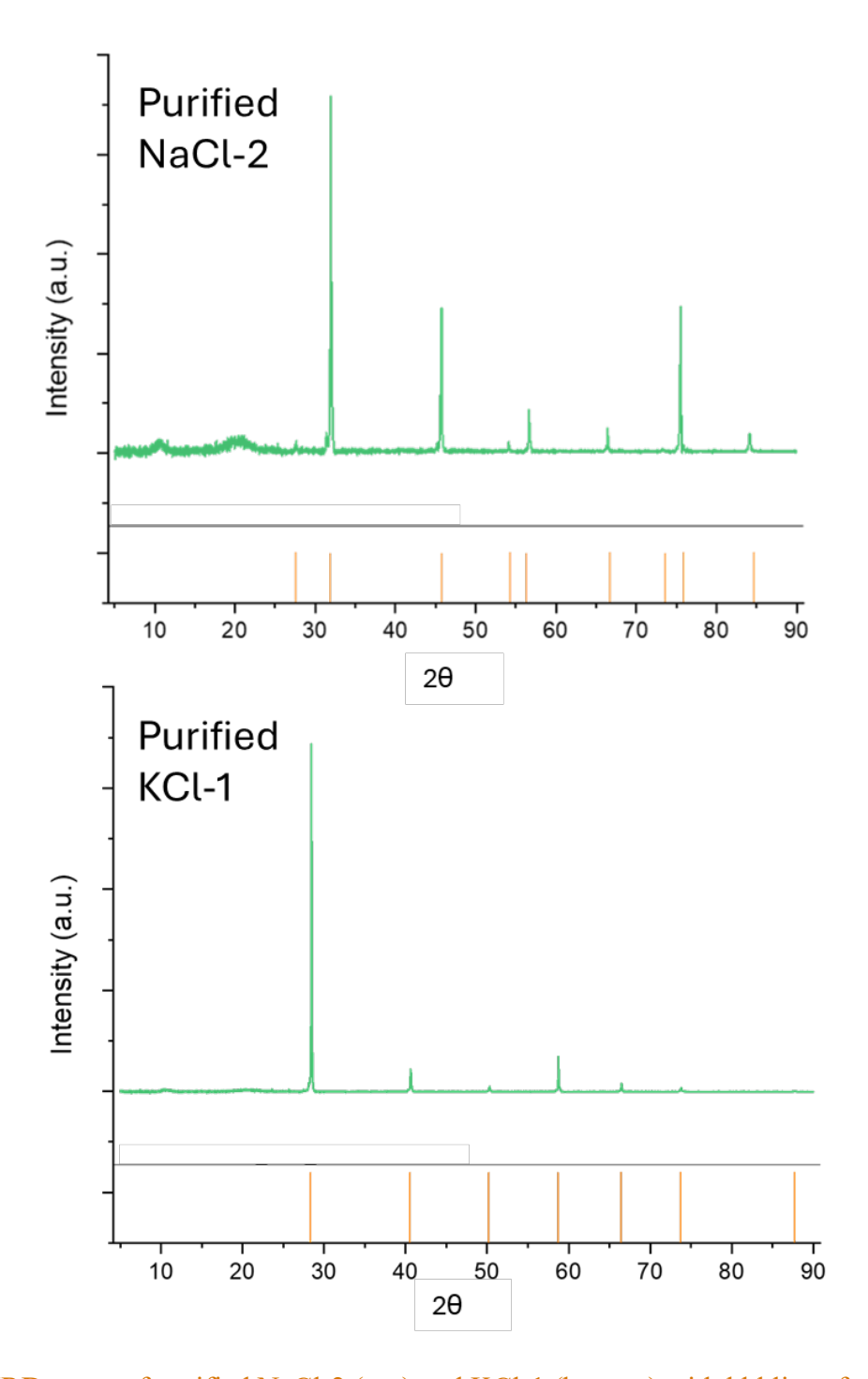


Figure 13. XRD scans of purified NaCl-2 (top) and KCl-1 (bottom) with hkl lines for peak identification in orange.

# 3.4 Determination of Melting Point

To assess the potential effects of fluid inclusions on thermophysical properties and to determine the efficacy of the hydrochlorination purification method, melting point was measured by differential thermal analysis (DTA) and thermomechanical analysis (TMA). This physical

property was chosen due to the relative ease of measuring and its hypothesized sensitivity to water contents.

The results of the melting point analysis for DTA are shown in Figure 14. Four samples were measured, two sodium chlorides and two potassium chlorides, each as a non-purified and purified pair from the same stock salt. Melting is an endothermic process and is evidenced in the DTA curve by the sharp drop in the signal (Fig. 14). For simplicity the TGA mass curves are not shown in Figure 14, but it should be noted only a slight mass loss was detected at initial melt onset. Future work will investigate if this is related to mass loss due to liberation of water contained within the inclusions or some other source.

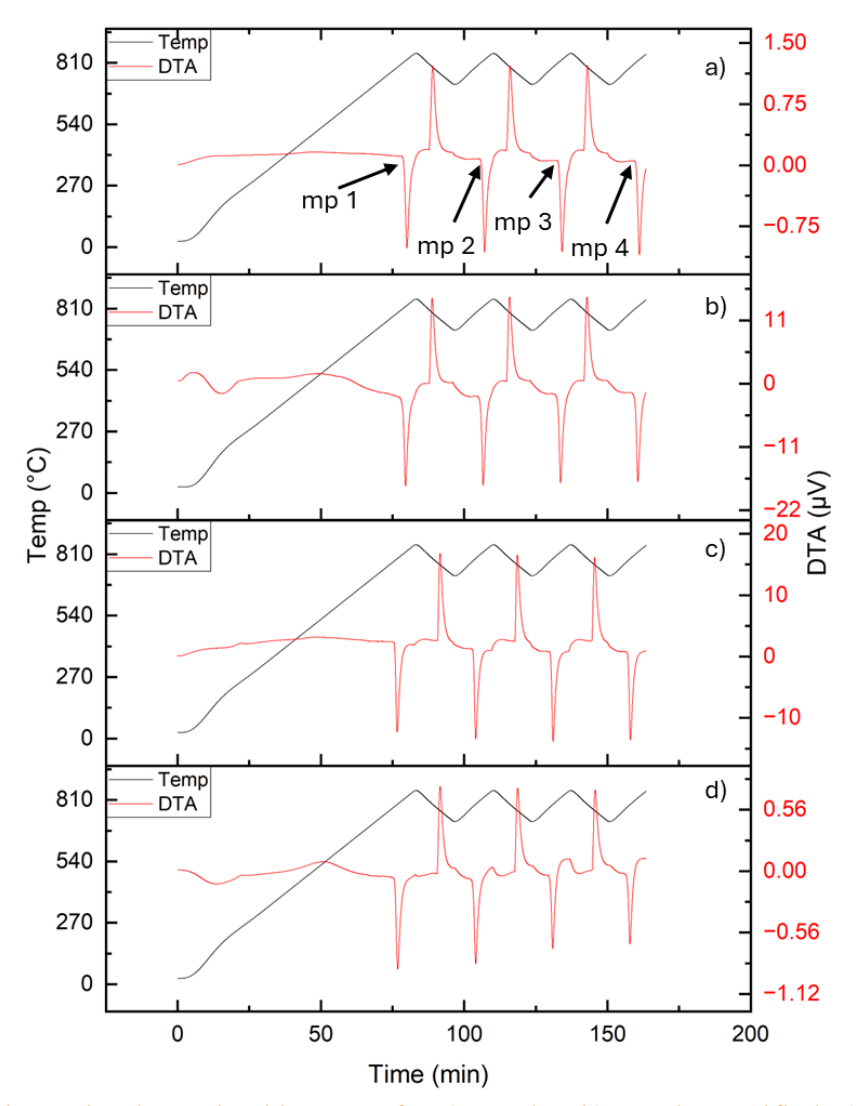


Figure 14. Melting point determined by DTA for a) NaCl-2, b) NaCl-2 Purified, c) KCl-1, and d) KCl-1 Purified. Multiple melting points annotated in the top panel but apply to all panels.

Results of melting point temperature derived by TMA are shown in Figure 15. Only two samples could be run due to time constraints, NaCl-1 and NaCl-2 purified. Additionally, the limited onhand supply of NaCl-1 precluded it from being purified via hydrochlorination. The volume change associated with phase change from solid to liquid manifests as a sharp drop in the dL/Lo

signal in the TMA, where dL/Lo is the unitless ratio between the change in length divided by the initial length (Fig. 15).

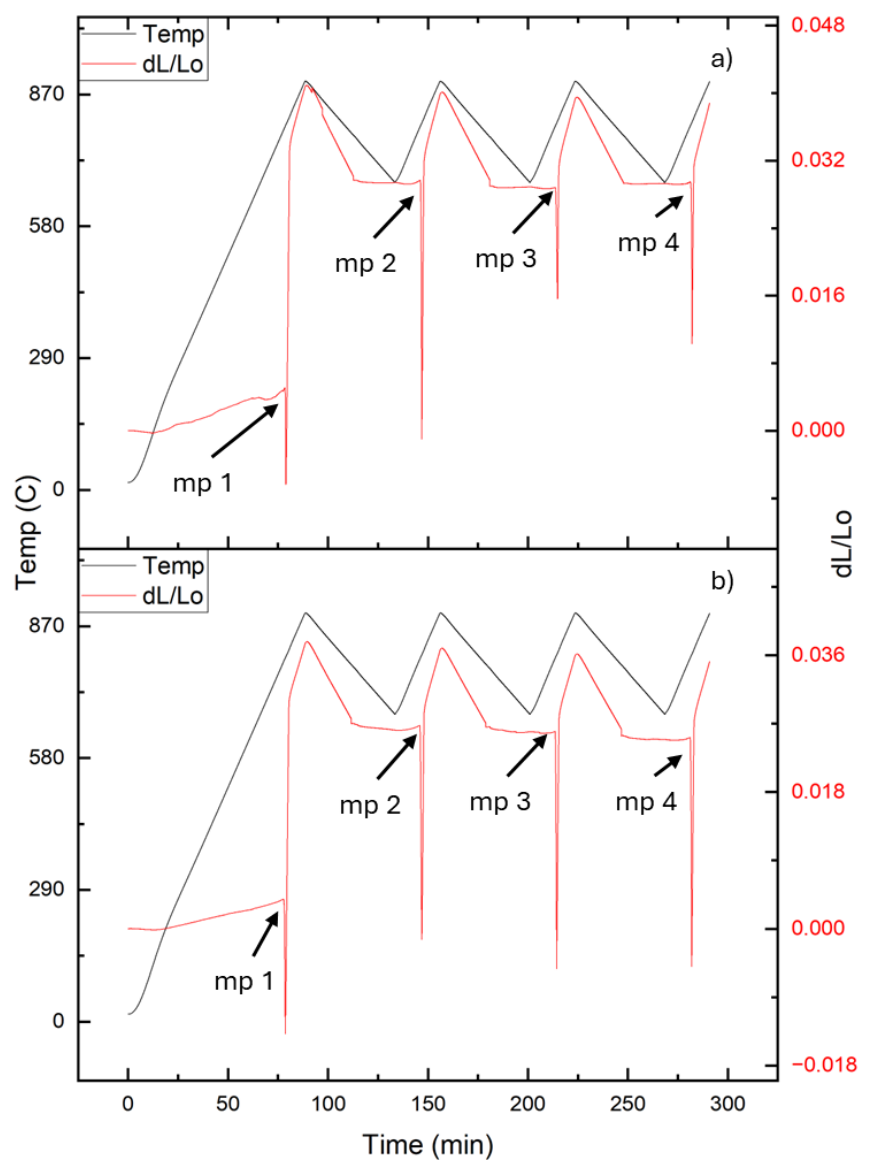


Figure 15. Melting point determined by TMA for a) NaCl-1 and b) NaCl-2 Purified. Positions in dL/Lo curve (red) showing melting point are annotated.

Results from both methods are tabulated in Table 3. It was hypothesized that the water contained within the inclusions would only affect the first melting point. After being liberated upon first melt, the water would be swept away by the argon cover gas. Upon solidification after dropping below the melting point, the salt would be free of water and thus any subsequent melts would be representative of the melting point of the pure salt. Based on the DTA results, it does not appear that the presence of fluid inclusions made a measurable impact to the melting point temperature. However, the TMA results suggest a different interpretation may be possible. The salt NaCl-1, which of the sodium chloride salts tested was determined to have the largest volume of fluid inclusions, does show a 5.3 °C depression in the melting point temperature as measured by

TMA. However, a similar magnitude depression in the melting point temperature was also measured for the NaCl-2 Purified salt. Potassium chloride samples KCl-1 and KCl-1 purified show no statistical difference in the first melt and subsequent melt temperatures. The large increase in the dL/Lo signal after the first melt is an artifact of the geometry of the sample, crucible cross-sectional area, volume change upon melting of the salt, and the movement of the plunger after the thaw/freeze cycle. It does not have to do with different water content between the first and subsequent melts.

Table 3. Comparison of measured melting points between DTA and TMA, respectively.

Salt	First Melt Temperature (°C)	Average Temperature of Subsequent Melts (°C)	Cited Melting Point (°C)
NaCI-1 As Received	807.1; 798.7	807.2; 804.0	800.9 ± 2.1 <sup>1</sup>
NaCI-2 As Received	806.9;	807.1;	
NaCI-2 Purified	803.6; 797.6	803.7; 803.1	
KCI-1 As Received	775.1; N/A	775.5; N/A	775.1 ± 2.1 <sup>1</sup>
KCI-1 Purified	775.7; N/A	774; N/A	

<sup>&</sup>lt;sup>1</sup>(Janz et al., 1975)

More work is needed to better understand the implication of the melting point results. Currently, it is unclear if the observed depression is related to the presence of fluid inclusions. For the TMA results, it is possible the apparent depression in measured melting point is an artifact of the measurement technique, but the system was carefully calibrated before analysis. Another possibility relates to the total mass of the salts measured versus the sensitivity of the techniques used. For example, using a nominal density 1.0 g/cm³ for the water within the inclusions, a nominal density of 2.16 g/cm³ for NaCl at room temperature, a 0.25 g sample aliquot, and the calculated total volume of water for NaCl-1 Grain 1 of 1.71 vol % (highest estimate), the total mass of water in the sample is approximately 2 mg. It is possible this mass of water does not affect the melting point to a degree that is resolvable by the DTA or TMA. A simple test would be to increase the mass of sample used in each method to find the threshold mass needed to produce a measurable result.

# 4.0 Conclusions

This work presents for the first time a detailed and targeted study of fluid inclusions in synthetic alkali chloride salts for the purpose of molten salt research. Number, size and total volume of inclusions vary both grain-to-grain and across manufacturers, suggesting differing synthetic process pathways. Observable inclusions typically exist as two-phase inclusions consisting of both a liquid and gas phase. Long-axis XY dimensions typically range between ~3-15 µm. Two methods were developed to determine the volume of the inclusions, a manual method requiring direct human determination and a supervised-ML technique. Preliminary results suggest the salts investigated contain ~0.02-1.7 volume percent water as fluid inclusions.

A new capability at PNNL was developed utilizing micro-Raman spectroscopy to non-destructively measure the contents of inclusions, or more generally features below the surface of the material in which it is hosted. Comparisons between purified salts and regions observed to be inclusion free differ in the measured Raman spectra from those of zones targeting fluid inclusions. Inclusions were verified to contain water evidenced by broad Raman spectral features centered around *ca*. 3400 cm<sup>-1</sup>. Depth profiles starting above the target inclusion, moving down into the inclusion, and finally below the inclusion show a commensurate increase then decrease in the measured intensity of the spectral feature associated with water near *ca*. 3400 cm<sup>-1</sup>.

Two purification methods were employed in the attempt to rid the host salt of their fluid inclusions. Vacuum drying at 100 and 200 °C for a duration of 8 hours was found to be inadequate at removing fluid inclusions. Hydrochlorination was used to successfully remove the fluid inclusions.

Melting point data were collected for pre- and post-hydrochlorinated sodium and potassium chloride salts, i.e., inclusion-bearing and inclusion-free. The results are mixed between the two methods, with data derived by TMA suggesting there is a *ca.* 5 °C depression in NaCl salts containing fluid inclusions vs inclusion free salt. However, a similar trend was observed in purified salts, thus currently more work is needed to delineate this discrepancy.

It is recommended that any salt purchased from commercial vendors be interrogated for the existence of fluid inclusions. They provide a significant unwanted source of water, which may lead to compromised and misleading thermophysical data, increased corrosion of container materials, and corrosion products in the salt. The hydrochlorination method was found to eliminate fluid inclusions from the salt. Similar purification methods should be developed and implemented for fluoride salts.

Conclusions 22

# 5.0 References

- Bodnar, RJ, CW Burnham, and SM Sterner. "Synthetic Fluid Inclusions in Natural Quartz. Iii. Determination of Phase Equilibrium Properties in the System H2o-Nacl to 1000 C and 1500 Bars." *Geochimica et Cosmochimica Acta* 49, no. 9 (1985): 1861-73.
- Cooper, James, Lionel Borne, and Gérard Coquerel. "Antisolvent Addition: An Effective Method of Controlled Fluid Inclusion Formation in Rdx Crystals." *Crystal Growth & Design* 20, no. 11 (2020): 7120-28.
- Fernández, Angel G, and Luisa F Cabeza. "Corrosion Evaluation of Eutectic Chloride Molten Salt for New Generation of Csp Plants. Part 2: Materials Screening Performance." Journal of Energy Storage 29 (2020): 101381.
- He, Kaiming, Haoqi Fan, Yuxin Wu, Saining Xie, and Ross Girshick. "Momentum Contrast for Unsupervised Visual Representation Learning." Paper presented at the Proceedings of the IEEE/CVF conference on computer vision and pattern recognition, 2020.
- He, Kaiming, Xiangyu Zhang, Shaoqing Ren, and Jian Sun. "Deep Residual Learning for Image Recognition." Paper presented at the Proceedings of the IEEE conference on computer vision and pattern recognition, 2016.
- Hurai, Vratislav, Monika Huraiová, Marek Slobodník, and Rainer Thomas. *Geofluids: Developments in Microthermometry, Spectroscopy, Thermodynamics, and Stable Isotopes.* Elsevier, 2015.
- Indacochea, JE, JL Smith, KR Litko, and EJ Karell. "Corrosion Performance of Ferrous and Refractory Metals in Molten Salts under Reducing Conditions." *Journal of Materials Research* 14, no. 5 (1999): 1990-95.
- International, ASTM. Standard Test Method for Temperature Calibration of Thermomechanical Analyzers. ASTM E1363-23. West Conshohocken, PA: ASTM International, 2023-08-15, 2023.
- Janz, G. J., R. P. T. Tomkins, C. B. Allen, J. R. Downey Jr., G. L. Garner, U. Krebs, and S. K. Singer. "Molten Salts: Volume 4, Part 2, Chlorides and Mixtures—Electrical Conductance, Density, Viscosity, and Surface Tension Data." *Journal of Physical and Chemical Reference Data* 4, no. 4 (1975): 871-1178. <a href="https://doi.org/10.1063/1.555527">https://doi.org/doi/abs/10.1063/1.555527</a>. https://doi.org/doi/abs/10.1063/1.555527.
- Makovsky, Kyle A., Michaella S. Harris, Ji-Hye Seo, Kent Powell Detrick, Jose Marcial, Dallin J. Barton, and Jacqueline I Royer. *Experimental Investigation into Select Thermophysical Properties of the Potassium-Magnesium Chloride Salt System for Molten Salt Reactors*. Pacific Northwest National Laboratory (Richland, WA: 2024).
- Marc, Laureline, Chrystal Lopes, Jean-Marie Schneider, Morgane Sanselme, and Gérard Coquerel. "Impact of a Partial Solid Solution and Water Molecules on the Formation of Fibrous Crystals and Fluid Inclusions." *Crystals* 11, no. 10 (2021): 1188.
- Maricle, D. L., and D. N. Hume. *A New Method for Preparing Hydroxide-Free Alkali Chloride Melts.* (United States: 31 1958). https://www.osti.gov/biblio/4197980.
- Raiman, Stephen S., Dino Sulejmanovic, J. Matthew Kurley, JoJo Lee, Cory G. Parker, and Bruce A. Pint. *Technical Assessment of Materials Compatibility in Molten Salt Reactors*. Material Science and Technology Division, Oak Ridge National Laboratory (Oak Ridge, TN: 2021).

References 23

- Rippy, Kerry, Liam Witteman, Patrick R Taylor, and Judith C Vidal. "Predicting and Understanding Corrosion in Molten Chloride Salts." *MRS Advances* 8, no. 15 (2023): 855-59.
- Roedder, Edwin. "Volume 12: Fluid Inclusions." Rev. Mineral 12 (1984): 644.
- Ronneberger, Olaf, Philipp Fischer, and Thomas Brox. "U-Net: Convolutional Networks for Biomedical Image Segmentation." Paper presented at the International Conference on Medical image computing and computer-assisted intervention, 2015.
- Russakovsky, Olga, Jia Deng, Hao Su, Jonathan Krause, Sanjeev Satheesh, Sean Ma, Zhiheng Huang, et al. "Imagenet Large Scale Visual Recognition Challenge." *International journal of computer vision* 115, no. 3 (2015): 211-52.
- Schneider, Caroline A., Wayne S. Rasband, and Kevin W. Eliceiri. "Nih Image to Imagej: 25 Years of Image Analysis." *Nature Methods* 9, no. 7 (2012/07/01 2012): 671-75. https://doi.org/10.1038/nmeth.2089. https://doi.org/10.1038/nmeth.2089.
- van den Kerkhof, Alfons, Andreas Kronz, and Klaus Simon. "Deciphering Fluid Inclusions in High-Grade Rocks." *Geoscience Frontiers* 5, no. 5 (2014): 683-95.
- Witteman, Liam, Kerry Rippy, Patrick Taylor, and Judith Vidal. "Continuous Purification of Molten Chloride Salt: Electrochemical Behavior of Mgohel Reduction." Journal of The Electrochemical Society 170, no. 6 (2023): 063502.

References 24

# Pacific Northwest National Laboratory

902 Battelle Boulevard P.O. Box 999 Richland, WA 99354

1-888-375-PNNL (7665)

www.pnnl.gov